Conductive, tough, hydrophilic poly(vinyl alcohol)/graphene hybrid fibers for wearable supercapacitors

Shaohua Chen, Wujun Ma, Hengxue Xiang, Yanhua Cheng, Shengyuan Yang, Wei Weng, Meifang Zhu[*]

State Key Laboratory for Modification of Chemical Fibers and Polymer Materials, College of Materials Science and Engineering, Donghua University, Shanghai 201620, PR China

HIGHLIGHTS

- Homogeneous mobile PVA/GO dispersions without gelation were successfully obtained.
- Continuous PVA/RGO hybrid fibers were produced by spinning and chemical reduction.
- The hybrid fibers shows obviously higher toughness, hydrophilicity and capacitance.
- A yarn supercapacitor was assembled and exhibits an energy density of 5.97 mW h cm^{-3}.
- The supercapacitor is flexible and robust enough to be weaved into a textile.

GRAPHICAL ABSTRACT
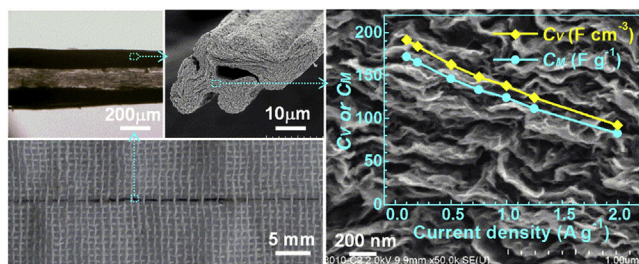
ABSTRACT

Graphene fibers based flexible supercapacitors have great potential as wearable power sources for textile electronics. However, their electrochemical performance is limited by the serious stacking of graphene sheets and their hydrophobicity in aqueous electrolytes. Meanwhile, their brittleness is unfavorable for practical application. Incorporation of nanofillers into graphene fibers has been proved effective for enhancing their capacitance, whereas often leading to deteriorated mechanical strength. Herein we demonstrate that the strength, toughness and capacitive performance of graphene-based fibers can be significantly enhanced simultaneously, simply by incorporating hydrophilic poly(vinyl alcohol) (PVA) into a non-liquid-crystalline graphene oxide (GO) dispersion before wet spinning and chemical reduction. The structure and properties of the resulted PVA/graphene hybrid fibers are systematically investigated, and the mechanism behind these enhancements is discussed in detail. The hybrid fiber with a PVA/GO weight ratio of 10/90 possesses a strength of 186 MPa, a toughness of 11.3 J cm^{-3}, and a capacitance of 241 F cm^{-3} in 1 M H$_2$SO$_4$. A solid-state yarn supercapacitor assembled from these fibers exhibits a device energy of 5.97 mW h cm^{-3}, and features excellent flexibility and bending stability. This device is robust enough to be integrated into textile and thus promising as wearable power supply for smart textiles.

* Corresponding author.
  E-mail address: zhumf@dhu.edu.cn (M. Zhu).

1. Introduction

Smart textiles can integrate a lot of functional electronic components such as sensors, heating/illuminating elements, wireless modules, and actuators. Hence they will find various applications in the fields of health/sports/environmental monitoring [1], professional and military activities [2,3], and entertainment and fashion [4]. However, one major challenge for smart textiles is the development of wearable power supply that is flexible, robust and durable. Fiber-based supercapacitors (FSCs) have been considered as ideal candidates for this end, due to their flexibility and readily compatibility with textile processing [5]. In the last decade, a variety of intrinsic and modified fibers have been explored for this purpose, including carbon fibers [6—8], carbon nanotube (CNT) fibers [5,9,10], and graphene fibers [11—17]. Recently, great progress has been made in terms of energy density and power density [15,18]. Although showing lower mechanical strength and electrical conductivity than carbon fibers and CNT fibers, graphene fibers exhibit significantly higher specific capacitance due to graphene's ultrahigh specific surface area. Meanwhile, the cost of graphene fibers would be much lower, considering the abundance of its raw material-natural graphite, and the scalability of its production method-wet spinning from graphene oxide (GO) dispersion followed by reduction [19—21]. Therefore, graphene-based fibers have a greater potential in wearable energy storage.

Unfortunately, the specific capacitance of graphene fibers in aqueous electrolyte is far from the theoretical value of a single graphene sheet [12,13], due to the $\pi-\pi$ stacking and hydrophobicity of graphene sheets. Two main strategies for the capacitance enhancement of graphene-based electrodes are to create a porous structure [22—25] and to improve the affinity to the electrolyte [26—29], which can also apply to graphene-based electrodes. In our previous work, we demonstrated that both the porous structure and the wettability of graphene fibers play important roles on the electrochemical performance [20]. The benefit of a porous structure has been proved by the dramatically improved capacitive performance of an all-graphene fiber with porous sheath [12,30] and a highly porous neat graphene fiber [11]. Hybrid porous graphene fibers also show significantly enhanced capacitance, because of the spacer effect of various nanofillers such as MoS_2 and CNT [15,31—33]. However, the mechanical strength of both neat and hybrid porous graphene fibers are obviously deteriorated due to the presence of plenty of pores. Therefore, it is a great challenge to simultaneously enhance the mechanical and electrochemical property to meet the requirements of smart textiles.

It has been reported that the strength and toughness of CNT fibers can be enhanced by infiltration polymers into the fibers during or after the spinning process, such as poly(methyl methacrylate) [34], polyethylene [35] and poly(vinyl alcohol) (PVA) [36,37]. Low cost PVA is highly hydrophilic and compatible with GO, and could inhibit the stacking of GO sheets and hence reduced GO (RGO) sheets. Thus the mechanical and capacitive performances of RGO fibers would probably be improved by hybridizing RGO with appropriate amount of PVA. Gao's group has successfully assembled PVA-coated chemically-reduced graphene (CRG@PVA) hydrogel into nacre-mimicking CRG@PVA fibers with enhanced strength [38]. However, the preparation of CRG@PVA building blocks is time-consuming, and the low content of CRG (<50 wt%) in the fiber is not favorable for supercapacitor applications. In this work, conductive, tough and hydrophilic PVA/RGO hybrid fibers with high content of RGO were easily obtained by fast mixing of PVA solution with non-liquid-crystalline GO dispersion followed by continuous wet-spinning and chemical reduction. Results show that their mechanical strength, toughness, hydrophilicity and electrochemical performance are simultaneously enhanced at a significant degree compared with the neat RGO fibers. A solid-state yarn supercapacitor assembled from these hybrid fibers exhibits superior volumetric energy densities to the devices assembled from other reported graphene-based fibers. Meanwhile, this device is flexible and robust enough to be integrated into a textile, demonstrating its potential in wearable energy storage for smart textiles.

2. Experimental methods

2.1. Preparation of the RGO and PVA/RGO fibers

Graphite oxide (GtO) was prepared from flake graphite (1000 mesh, Shanghai Yifan Graphite) by Hummers' method [39] according to our previous report [20]. 2 g GtO was added into 98 g deionized water and exfoliated with a digital ultrasonic processor (S-450D, Branson) for 1 h. The resulting 2 wt% graphene oxide (GO) dispersion was liquid-crystalline (as confirmed by polarized optical microscope) with pH $\approx$ 2, and was denoted as pristine GO (PGO) dispersion. The basified GO (BGO) dispersion was obtained by addition of 10 M NaOH solution dropwise into 80 g PGO dispersion under stirring until the pH was around 11. After a further sonication for 5 min, the BGO dispersion was non-liquid-crystalline and flowed very easily [20]. A 2 wt% PVA solution was obtained by dissolving 1 g PVA (polymerization degree = 1700, saponification degree = 99%, Shanghai Petroleum) in 49 g deionized water at 95 °C for 1 h. Then it was mixed with the BGO dispersion at different PVA/GO weight ratios of 5/95, 10/90, 20/80 and 30/70 under sonication for 15 min. All the final PVA/BGO dispersions are homogeneous and easy-flowing, and are suitable for wet-spinning. In contrast, an immobile gel was formed when the PVA solution was blended with the PGO dispersion at a weight ratio of 30/70, and is not qualified for wet-spinning.

The RGO and PVA/RGO fibers were prepared by continuous wet-spinning followed by chemical reduction in the same way as our previous work [20]. The BGO and PVA/BGO dispersions were used as the spinning dope, respectively, and the jet stretch ratio was all controlled at 1.0. In a typical process, a PVA/BGO dispersion was loaded into a 10-ml syringe and injected into a rotating acetic acid bath through a 27 G needle at a speed of 1.5 m min^{-1}. The coagulated wet PVA/GO fiber was immediately drawn out of the bath, dried by a vertically-positioned infrared heater, and collected onto a winding pipe (Fig. 1g). Note that the simultaneous drying process guarantees that the GO and PVA/GO fibers adhere neither to themselves nor to the pipe. All GO and PVA/GO fibers were reduced in an aqueous HI solution (45%, Sinopharm) at 95 °C for 8 h [40], then washed alternatively by water and acetic acid for three times, and finally dried at 60 °C for 12 h in vacuum. The PVA/GO and PVA/RGO fibers are respectively named as P_xG_y and RP_xG_y fibers, where x and y are the percent weight ratio of PVA and GO in the dispersion for wet-spinning, respectively.

2.2. Assembly of a PVA/RGO yarn supercapacitor

A yarn supercapacitor was assembled from two bundles of PVA/RGO fibers as the working electrodes and a poly(ethylene terephthalate) (PET) yarn as the supporting substrate. Two bundles of five $RP_{10}G_{90}$ fibers (length = 1.7 cm) were arranged in parallel on a polypropylene sheet such that the length of the middle overlapped part is 1.5 cm. The PET yarn (length = 15 cm) was straightened, inserted closely between the two bundles, and fastened on the polypropylene sheet. The overhang ends (~0.1 cm) of the two bundles were adhered to the PET yarn by silver paste. Then the middle overlapped part (length = 1.5 cm) was carefully coated with PVA/H_2SO_4/H_2O (1/1/10 in weight) gel electrolyte, so that a gap of
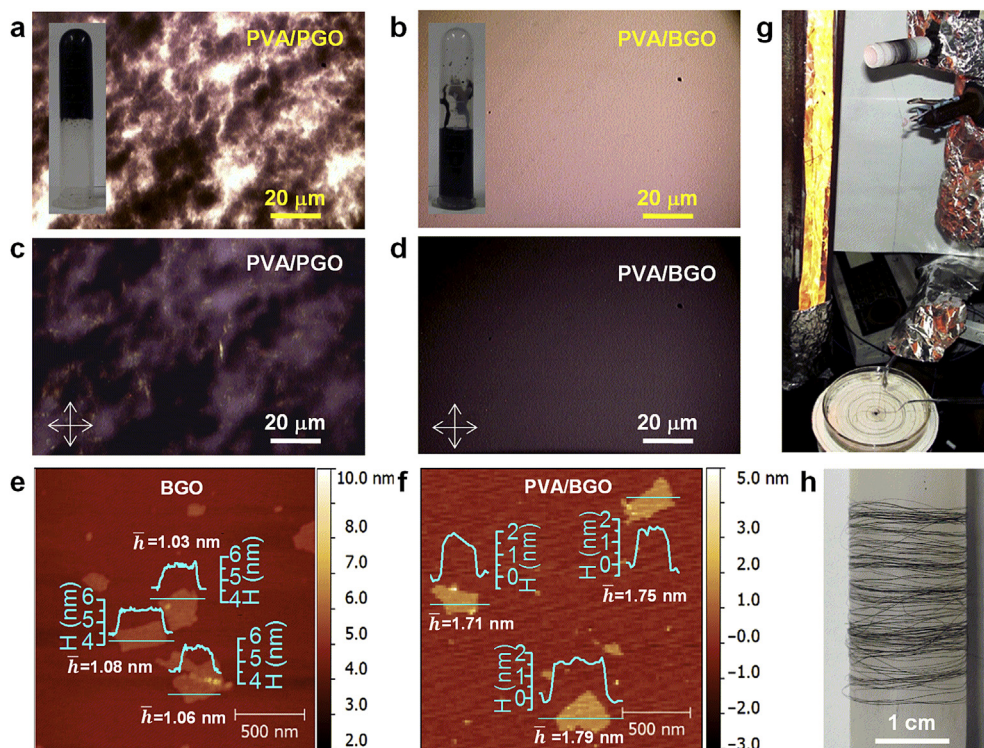
Fig. 1. Characteristics of the PVA/GO dispersions, the spinning process and the typical PVA/RGO hybrid fiber. (**a**–**d**) OM images of (**a**, **c**) the PVA/PGO and (**b**, **d**) PVA/BGO dispersions under (**a**, **b**) normal light and (**c**, **d**) polarized light. The PVA/GO ratio is 30/70 and the total solid content is 2 wt%. Insets are photos of the dispersions in centrifuge tubes with upside down. (**e**, **f**) Typical AFM images of (**e**) BGO sheets and (**f**) PVA/BGO (weight ratio = 30/70) sheets. Insets are height profiles of the corresponding lines. (**g**) Photo of the continuous wet-spinning process. The dope is injected through a needle into the rotating coagulant (in the petri-dish), and solidifies into a fiber, which is dried by the infrared heater and collected onto a plastic pipe. (**h**) Photo of a scroll of the $RP_{10}G_{90}$ fiber.

~0.1 cm was left between the silver paste and the electrolyte. After drying the electrolyte with an infrared heater for 3 min, a flexible solid-state yarn supercapacitor was obtained by peeling off from the polypropylene sheet.

2.3. Characterizations

The PVA/PGO and PVA/BGO dispersions as well as the yarn supercapacitor were examined by an Alphaphot-2 optical microscope (OM, Nikon, Japan) under normal or polarized light. Atomic force microscope (AFM) images were obtained by a NanoScope IIIa MultiMode AFM (Veeco Instruments, USA). The X-ray photoelectron spectra (XPS) were collected on an Axis Ultra DLD spectrometer (Kratos Analytical, UK) using a monochromatic Al Kα source. The Fourier transform infrared (FTIR) spectra were recorded from a Nicolet NEXUS-670 spectrometer (Thermo Scientific, USA). The morphology of the fibers were observed by an SU8010 filed-emission scanning electron microscope (SEM, Hitachi, Japan). The average area, diameter and perimeter of the fiber cross-section were analyzed from the SEM images by an Image-Pro Plus software (Media Cybernetics). The X-ray diffraction (XRD) spectra of the fiber powder were collected on a D/max 2550 PC diffractometer (Rigaku, Japan) with a Cu Kα radiation. The nanostructure of PVA/RGO hybrids were observed on a JEM-2100 transmission electron microscope (TEM) (JEOL, Japan). The $RP_{30}G_{70}$ fiber was pulverized into powder, ultrasonicated in a water/ethanol mixture (volume ratio = 1/1) for 3 h, and finally centrifuged at 3000 rpm for 30 min. The upper suspension was dropped onto a lacey-carbon coated copper grid for TEM observation after drying.

The linear density of each kind of fiber was calculated by dividing the mass of a filament with its length (~5 m), where the mass was obtained from an XS microbalance (Mettler Toledo, USA). Mechanical tests were performed on an XQ-1A fiber tension tester (Shanghai New Fiber Instrument, China). The gauge length and extension rate were 10 mm and 2 mm min^{-1} respectively. The electrical resistance of the fibers with a uniform length of 1.8 cm was tested on a PC68 high resistance meter (Shanghai Cany Precision Instrument) by two probe method. At least 5 filaments for each kind of fiber were measured for both the mechanical and resistance tests, and average values of strength, modulus, toughness and electrical conductivity were calculated based on the cross-sectional area. The toughness is evaluated by the volume-specific work at fracture. The hydrophilicity of the fibers were investigated with a video-based optical contact angle measuring system (OCA 40 Micro, DataPhysics, Germany). A 50-nL deionized water droplet was dispensed onto the fiber surface, which was monitored by a high-speed camera. The contact angle at the very initial stage was reported.

The electrochemical performance was investigated on a CHI 660 E electrochemical workstation (Shanghai Chenhua). All the RGO and PVA/RGO fibers were firstly evaluated in a three-electrode cell, where the electrolyte, counter electrode and reference electrode are 1 M H_2SO_4 solution, Pt wire and Hg/Hg_2SO_4, respectively. For each kind of fiber, a bundle of five filaments was used as the free standing working electrode. In order to facilitate the link to the workstation, a stainless steel strip was used as the lead wire and connected to the fiber bundle end to end with silver paste. The silver paste was kept ~1 mm above the electrolyte surface to avoid its disturbance, and the immersion length of the fiber bundle was ~1.5 cm in the electrolyte. Cyclic voltammetry (CV) and galvanostatic charge-discharge (GCD) cycling were run from −0.6 V to 0.4 V with scan rates of 2—100 mV s^{-1} and current densities of

0.2–2 A g^{-1}, respectively. The electrochemical impedance spectroscopy (EIS) measurements were performed at open circuit potential with an AC amplitude of 5 mV and frequencies from 10 mHz to 1 MHz. The RP$_{10}$G$_{90}$ fiber with the best electrochemical performance was used to assemble a solid-state yarn supercapacitor. CV scans and GCD cycling tests were also performed for this device under both straight and bending state. The bending radius-R of the device during bending is controlled according to the equation: $R = 180 L/\pi\alpha$, where L and α are the length and bending angle (unit in degree) of the device, respectively.

The capacitance of a single electrode is calculated from the discharge portion of a full CV curve or a full GCD one as the following equations: $C = n(\int|I|dU)/v\Delta U$ or $C = nIT_d/(\Delta U - IR)$, where I is the current, U is the potential, v is the scan rate, ΔU is the potential window, IR is the potential drop, T_d is the discharge current, and n equals to 1 for three-electrode cell and 2 for two-electrode cell, respectively. The mass-, volume- and area-specific capacitance (denoted as C_M, C_V and C_A respectively) are obtained by dividing C with the mass-M, the volume-V and the outer surface area-A of a single electrode (a bundle of fibers), respectively. The volume and outer surface area of a single fiber is calculated by multiplying its length with its cross-sectional area and perimeter, respectively. The mass-based energy density (E_M) and power density (P_M) of the yarn supercapacitor device are determined from the discharge part of a GCD curve by the equations: $E_M = IT_d(\Delta U - IR)/4M$ and $P_M = I(\Delta U - IR)/4M$, respectively. The volume-based energy density was calculated similarly by replacing M with V.

3. Results & discussion

3.1. Characteristics of PVA/GO hybrid dispersions

Aqueous GO dispersions are liquid crystalline when the concentration is above the critical value [19,41,42], and have been used for wet-spinning to obtain continuous GO fibers [41,43], which can be converted to RGO fibers by chemical or physical reduction [19,11]. We found that the viscous liquid-crystalline PGO dispersion can be disrupted into a free-flowing non-liquid-crystalline (NLC) one after a simple basifying treatment, and the RGO fibers prepared from the NLC dispersion show superior electrochemical performance to that from the LC one [20]. It is interesting that the NLC BGO dispersion with much lower viscosity is more favorable for blending with a PVA solution. As can be seen in Fig. 1a–e, the PVA/PGO dispersion with a PVA/PGO weight ratio of 30/70 forms an immobile gel with many large aggregates, and could not be used for wet-spinning. The gelation of PVA with PGO or even RGO at appropriate weight ratios is also reported by Shi's and Gao's groups [44,38], and could be ascribed to the strong interactions between the oxygen containing groups (carboxyl, hydroxyl and epoxide) of GO sheets and hydroxyl ones of PVA [44,45]. In great contrast, the PVA/BGO dispersion with the same ratio is easy-flowing and no aggregates are observed in the OM images. The reason is that BGO sheets possess much higher negative charges than PGO ones, and produce much stronger electrostatic repulsion between neat or PVA-coated BGO sheets, leading to much weaker hydrogen-bond network [44,20]. Therefore, the viscosity would be decreased a lot. The AFM images (Fig. 1e and f) show that the heights of PVA/BGO sheets (1.7–1.8 nm) are much higher than those of neat BGO sheets (1.0–1.1 nm), indicating that PVA molecules are uniformly coated on the BGO sheets. It is believed that the homogenous PVA/BGO dispersions could guarantee a continuous spinning of PVA/GO fibers.

3.2. Structure of RGO and PVA/RGO fibers

Continuous RGO and PVA/RGO fibers were successfully obtained by wet-spinning of NLC BGO and PVA/BGO dispersions followed by chemical reduction. Fig. 1h shows a roll of typical PVA/RGO hybrid fiber-RP$_{10}$G$_{90}$, which could be obtained up to hundreds of meters long. The C1s XPS spectra (Fig. 2a) show that the PVA/GO hybrid fiber (i.e., P$_{10}$G$_{90}$) contains a lot of oxygen-containing groups, such as hydroxyl/ether/epoxy (286–287.5 eV) and carbonyl/carboxyl groups (287.5–290 eV). After reaction with HI solution, the intensities of hydroxyl/ether/epoxy groups become very weak, confirming the high reduction efficiency of HI [40]. The FTIR spectra (Fig. 2b) reveal that the RP$_{20}$G$_{80}$ hybrid fiber shows stronger peaks for O–H stretch (3700–3000 cm^{-1}) and bend (1600–1700 cm^{-1}) than the neat RGO fiber when normalized to the intensity of C–H stretch, indicating higher hydroxyl groups originated from PVA. Note that the peak for C–O stretch (1200–1000 cm^{-1}) become obviously stronger for both the RGO and RP$_{20}$G$_{80}$ fibers after reduction. The possible reason is that hydroxyl groups between GO sheets is condensed into ether bonds as a side reaction in the concentrated HI solution. Since PVA molecules possess plenty of hydroxyl groups, they would also condense with GO sheets and themselves, constructing extremely strong PVA-RGO interfaces with large amounts of covalent bonds (i.e. C–O–C and C–C–C bonds).

The morphology of the neat and hybrid fibers are shown by the SEM images in Fig. 3, and the characteristic parameters are summarized in Table 1. The neat RGO fiber shows coarse surface with large wrinkles and thin curvy belt-like cross-section with orderly stacked RGO sheets. By contrast, the PVA/RGO hybrid fibers exhibit surface with remarkably more and finer nano wrinkles, and different shaped cross-section with much thicker arms/walls and looser stacking of RGO sheets. It is also found that the nano wrinkles show higher alignment along the fiber axis at higher PVA content. These enormous differences are clearly originated from the contribution of PVA. Note that both neat PGO and BGO dispersions at 2 wt% can coagulate in acetic acid instantly, because the negatively charged -COO$^-$ groups on GO sheets can turn into –COOH groups in acetic acid and bind together through hydrogen-bonding [20]. However, the neat 2 wt% PVA solution cannot coagulate in acetic acid, because PVA molecules show good affinity to acetic acid through strong interaction between –OH and –COOH groups. Consequently, the mechanism for the PVA/GO hybrid fiber formation is based on the acetic acid-induced aggregation of BGO sheets and dehydration of the extruded flow. After reduction with HI solution, RGO and PVA/RGO fibers were resulted and inherited most of the structural characteristics of their precursor fibers [20]. For the spinning of GO fiber, a hard sheath would form on the surface of the extruded flow through the stacking of aggregated GO sheets, and would act as a barrier slowing the further diffusion of acetic acid and water, resulting in thin belt-like cross-section after drying. The wrinkles might be formed by outward self-scrolling of surface GO sheets with more negative charges on the inside than the outside due to the acidification by acetic acid [20].

As for the spinning of PVA/GO fibers, the PVA molecules can work as physical spacers between GO sheets and also chemical absorbent for acetic acid, thus offering plenty of nano channels for faster diffusion of acetic acid and water during the coagulation process compared with the spinning of GO fiber. On one hand, much more coagulating points would form on the surface, leading to a larger number and smaller size of nano wrinkles. The higher alignment of nano wrinkles with higher PVA content may be ascribed to higher viscosity of the corresponding PVA/BGO dispersion. On the other hand, more effective coagulation of the core would occur and lead to a cross-section with thicker walls after
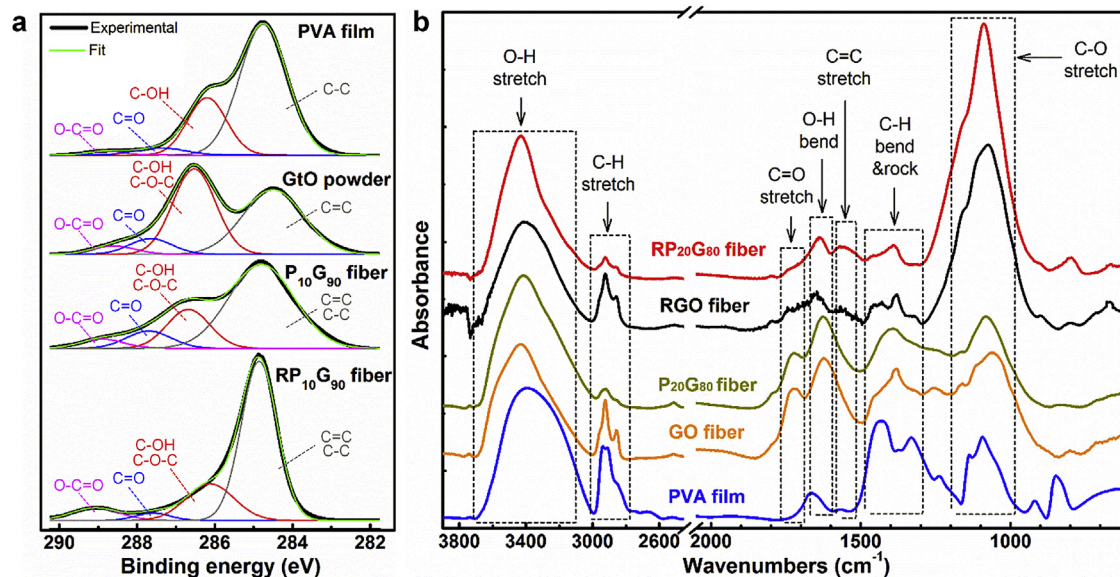
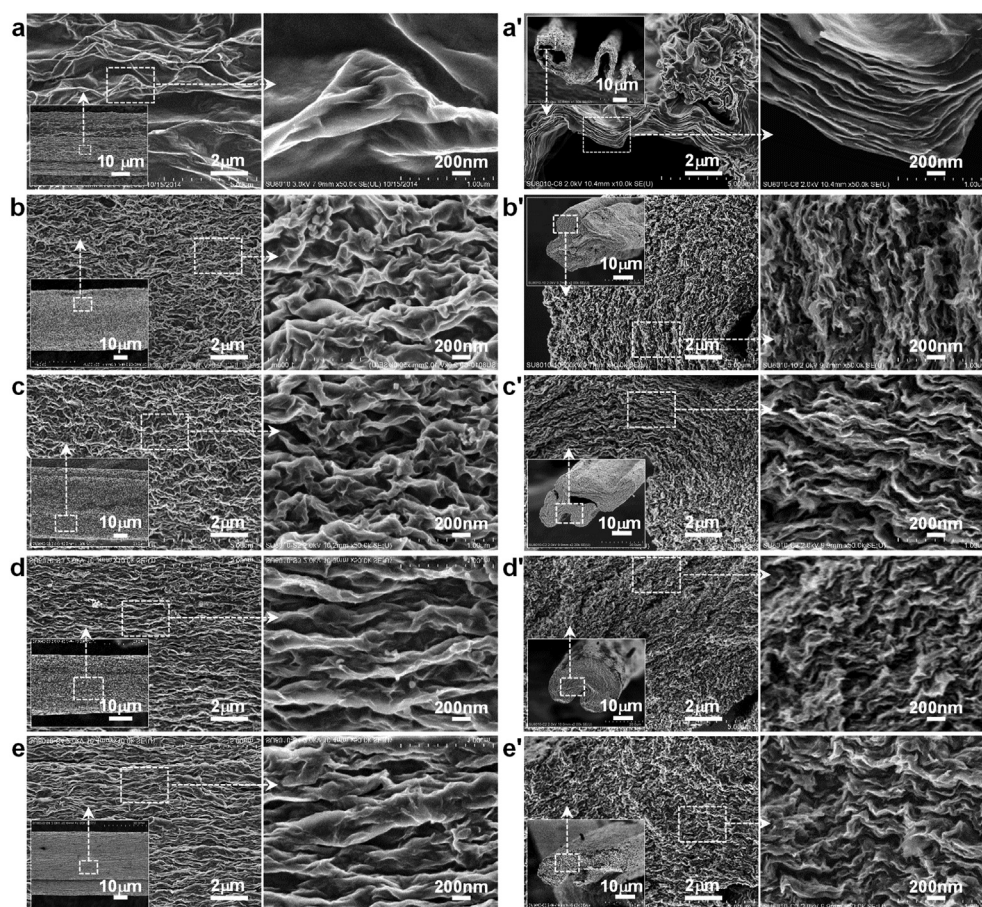**Fig. 2.** (a) High-resolution C1s XPS and (b) FTIR spectra of the raw materials and obtained fibers.

Fig. 3. Typical SEM images of (**a**−**e**) the surface and (**a′**−**e′**) the cross-section of RGO and PVA/RGO hybrid fibers. (**a**, **a′**) RGO fiber. (**b**, **b′**) RP_5G_{95} fiber. (**c**, **c′**) $RP_{10}G_{90}$ fiber. (**d**, **d′**) $RP_{20}G_{80}$ fiber. (**e**, **e′**) $RP_{30}G_{70}$ fiber.

drying. And the spacer effect of PVA molecules would result in looser stacking of GO and RGO sheets, which is proved by the XRD spectra and TEM images in Fig. 4. The presence of the diffraction peak of graphite-like (002) face indicates the stacking of RGO sheets in these fibers due to insufficient amount of PVA. However, its layer spacing increases almost linearly from 3.71 Å to 4.03 Å when the

Table 1
Summary on the morphology parameters of the RGO and PVA/RGO fibers.

Sample	Linear density [$\mu g\ cm^{-1}$]	Cross-section area [μm^2]	Diameter [μm]	Cross-section perimeter [μm]	Calculated density [$g\ cm^{-3}$]
RGO	4.32	544 ± 89	23.3 ± 4.3	229 ± 21	0.810 ± 0.125
RP_5G_{95}	8.40	738 ± 39	28.0 ± 1.0	144 ± 8	1.14 ± 0.06
$RP_{10}G_{90}$	7.07	633 ± 48	25.4 ± 5.2	166 ± 33	1.12 ± 0.09
$RP_{20}G_{80}$	9.97	662 ± 66	27.2 ± 2.0	108 ± 14	1.52 ± 0.15
$RP_{30}G_{70}$	8.78	681 ± 21	26.1 ± 1.2	136 ± 12	1.29 ± 0.04
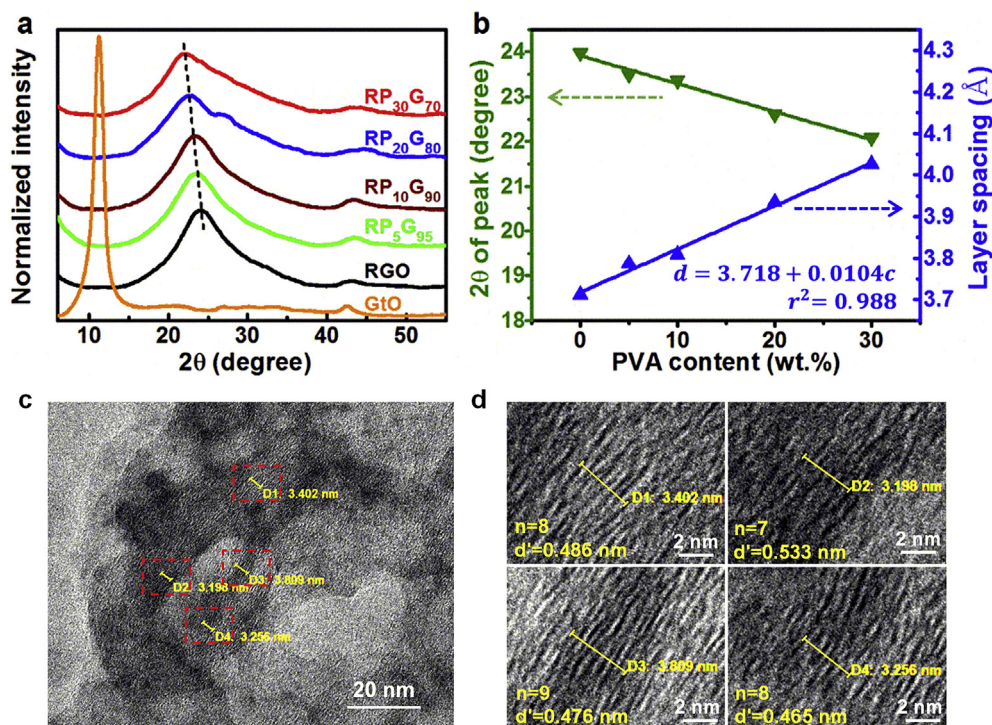
Fig. 4. (**a**) XRD spectra of the graphite oxide (GtO), RGO fiber and PVA/RGO fibers. (**b**) Dependence of the layer spacing of (002) face in hybrid fibers on the PVA content in the precursor fibers. (**c, d**) TEM images of pulverized PVA/RGO hybrids from the $RP_{30}G_{70}$ fiber at (c) low and (**d**) high magnification. The average layer-spacing d′ is calculated as $D/(n-1)$, where D and n represent the distance of the corresponding line and layer number of RGO sheets, respectively.

PVA content is increased from 0 wt% to 30 wt%. And the full width at half maximum is also increased, indicating that the lateral size of the stacking is decreased. Meanwhile, TEM images (Fig. 4d–e) of pulverized PVA/RGO hybrid fibers clearly show ordered layered structures, whose average layer-spacing (>0.46 nm) is much larger than that of RGO sheets. This implies the sandwiching of PVA molecules between the RGO sheets, which is the result of stacking and reduction of PVA-coated BGO sheets (Fig. 1f). Therefore, the addition of PVA decreases the degree of stacking of RGO sheets. We believe that the surface of PVA/RGO hybrid fibers with nano wrinkles would provide larger area for access to the electrolytes, and the loose inner structure would be favorable for fast diffusion and efficient adsorption of electrolyte ions.

3.3. Properties of RGO and PVA/RGO fibers

For wearable energy storage applications, the candidate fibers should be adequately strong, flexible and ductile to meet the requirements of textile processing as well as versatile wearing conditions. Fig. 5a displays the typical tensile stress-stain curves of the RGO and PVA/RGO fibers. The results show that the strength, modulus and toughness are simultaneously, remarkably enhanced when PVA is incorporated. The strength increases straightly from 95.6 MPa for the RGO fiber to 256 MPa by 168% for the $RP_{20}G_{80}$ fiber,

and slightly falls to 244 MPa for the $RP_{30}G_{70}$ fiber. Our $RP_{30}G_{70}$ and $RP_{20}G_{80}$ fibers are significantly stronger than most PVA/RGO composite films (43–138 MPa) [46–48], and much stronger than nacre-mimicking CRG@PVA fibers (161 MPa) [38]. And the modulus is steadily enhanced from 3.34 GPa for the RGO fiber to 8.44 GPa (by 153%) for the $RP_{30}G_{70}$ fiber. Meanwhile, the toughness shows an enormous improvement from 3.92 to 22.9 J cm^{-3} (by 485%) when the PVA content is increased to 20 wt%. The $RP_{10}G_{90}$ fiber also show significantly higher strength (186 MPa) and toughness (11.3 J cm^{-3}, 10.1 J g^{-1}) than the neat RGO fiber. Note that our $RP_{20}G_{80}$ fiber (22.9 J cm^{-3}) is much tougher than the nacre-mimicking CRG@PVA fiber (~3.0 J cm^{-3} and ~10 J cm^{-3} before and after soaking in water, respectively) [38]. These enhancements could mainly arise from the gap-filling effect of PVA molecules as indicated by obviously increased density, and the strong interface interaction between PVA molecules and RGO sheets as discussed earlier on the FTIR spectra. It is found that the $RP_{30}G_{70}$ fiber possess much lower toughness than the $RP_{20}G_{80}$ fiber. A possible reason is that excess PVA leads to too much cross-linking points between the RGO sheets and the PVA molecules and among PVA molecules themselves. As a result, the sliding between RGO sheets and the extension of PVA molecules could be greatly limited, which is evidenced by the much lower elongation rate at break.

Good electrical conductivity of the active material in the
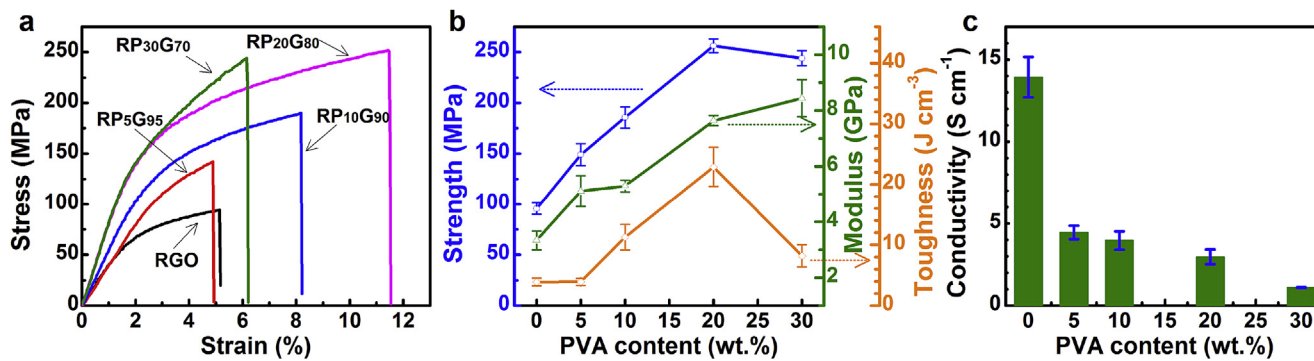
Fig. 5. Mechanical and electrical properties of the RGO and PVA/RGO fibers. (**a**) Typical tensile stress-strain curves. (**b**) Dependence of the strength, modulus and toughness on the PVA content. (**c**) Dependence of the electrical conductivity on the PVA content.

supercapacitor would favor a fast electron transport network and provide a good rate performance. The conductivity of the neat and hybrid fibers is shown in Fig. 5c. It can be seen that the conductivity decreases quickly from 13.9 S cm^{-1} for the neat RGO fiber to 4.45 S cm^{-1} for the RP$_5$G$_{95}$ fiber, then slowly to 2.97 S cm^{-1} for the RP$_{20}$G$_{80}$ fiber, and finally sharply again to 1.10 S cm^{-1} for the RP$_{30}$G$_{70}$ fiber. The possible reason is that the incorporation of insulative PVA would firstly fill the gaps among the edges of RGO sheets, and thus greatly block the direct electron transport pathway, which contributes mainly to the conductivity. Further increase of PVA would increase the layer spacing of RGO sheets, and slowly decrease the electron hopping among RGO sheets, which plays a minor role in the conductivity. However, the excess amount of PVA would entirely coat the RGO sheets and block those two ways for the electron transfer at the same time, leading to low conductivity and hence poor capacitive performance.

It has been recognized that the affinity of graphene-based electrodes to the electrolyte solution in a supercapacitor plays an important role in the access to and diffusion of electrolyte ions [20,27,29]. Most fiber-based supercapacitors work in aqueous electrolytes in either liquid or gel state, due to their environmental friendliness, safety and convenience. Therefore, we investigated the hydrophilicity of the RGO and PVA/RGO fibers through water contact angle tests. As shown in Fig. 6, the neat RGO fiber is hydrophobic with a water contact angle of 97°.On the contrary, all the PVA/RGO hybrid fibers are hydrophilic, with gradually decreased contact angles of 73°, 67°, 50° and 43° when the PVA content is increased from 5 to 30 wt%. This obvious improvement in the hydrophilicity is mainly originated from the hydrophilic hydroxyl groups of PVA molecules, as well as the newly formed ether groups after reaction in the HI solution. Note that aqueous PVA gel is widely used to support various electrolytes such as H$_3$PO$_4$, H$_2$SO$_4$ and LiCl for solid-state supercapacitors [5,33,49–51], because of its excellent affinity to these electrolytes. Consequently, it is believed that the PVA/RGO hybrid fibers would have excellent compatibility with PVA-based gel electrolyte, and would favor the transport of

the electrolyte ions across the fiber.

The electrochemical behavior of the RGO and PVA/RGO fibers were firstly evaluated in three-electrode cells with 1 M H$_2$SO$_4$ solution as the electrolyte. These fibers were used as free-standing working electrodes, and the results are shown in Fig. 7. For the CV tests at a scan rate of 2 mV s^{-1} (Fig. 7a), the neat RGO fiber exhibits a curve with very low area, corresponding to a specific capacitance of 9.24 F g^{-1}; while the PVA/RGO hybrid fibers display curves with significantly higher area despite of much lower conductivities, achieving a highest specific capacitance of 171 F g^{-1} for the RP$_{10}$G$_{90}$ fiber. Obvious redox peaks are observed for the RP$_{10}$G$_{90}$ and RP$_{20}$G$_{80}$ fibers, which can be stemmed from the reversible reduction and oxidation of oxygen-containing moieties such as carbonyl, carboxyl and phenolic groups on RGO sheets [52,20]. Fig. 7c shows that when the PVA content is increased from 0 to 30 wt%, the specific capacitance of these fibers firstly increases and then decreases, with maximum values at a PVA content of 10 wt%. The enormous capacitive enhancement enabled by PVA can be ascribed to four reasons. First, large quantities of nano wrinkles on the surface of the hybrid fibers provide much higher outer surface area for contacting with the electrolyte solution. Second, the hydrophilicity of the hybrid fibers would favor the intrusion of electrolyte ions into the fiber. Third, the spacer effect and the affinity of PVA to H$_2$SO$_4$ would benefit the ion diffusion across the fiber. Fourth, the looser stacking of RGO sheets provides significantly higher inner surface area for the adsorption of electrolyte ions and exposes much more number of oxygen-containing groups, thus greatly contributing to the electric double layer capacitance and pseudo-capacitance, respectively. Nevertheless, excess amount of PVA not only decreases the electron conductivity, but would also fill the gaps densely and cross-link the RGO sheets tightly, leaving less room for the ion diffusion through the fiber. These explanations are supported by the result of EIS in Fig. 7d. It can be seen that the neat RGO fiber shows the highest impedance at all frequencies, and the charge-transfer resistance (the diameter of the semicircle) decreases in the order of RP$_5$G$_{95}$, RP$_{30}$G$_{70}$, RP$_{20}$G80 and RP$_{10}$G$_{90}$.
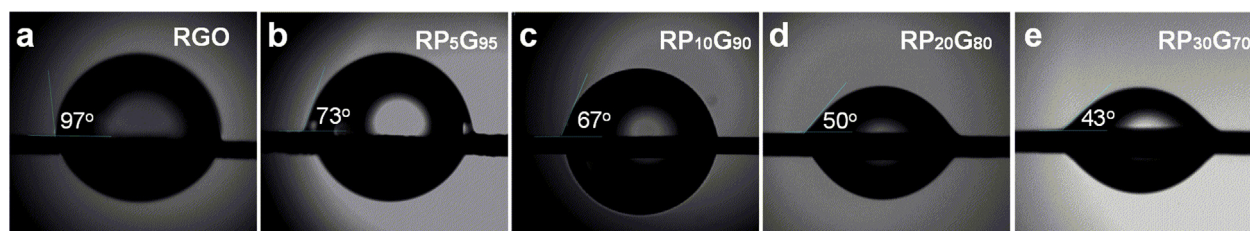
Fig. 6. Optical microscopic images of a water droplet on the RGO fiber and PVA/RGO hybrid fibers.
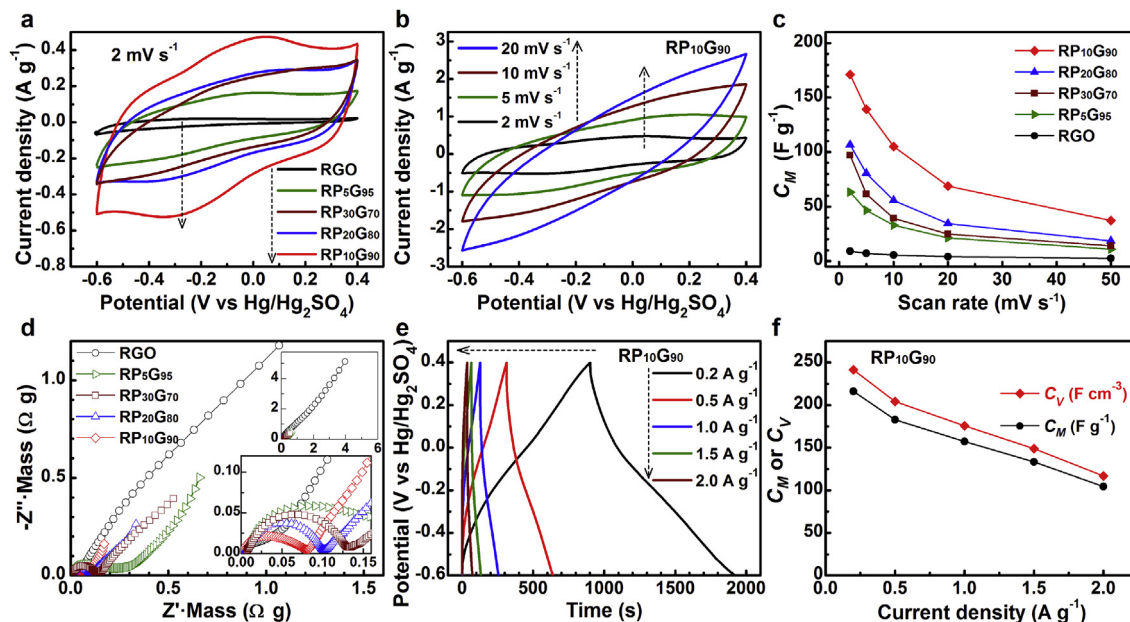
Fig. 7. Electrochemical properties of the RGO fiber and PVA/RGO hybrid fibers. (**a**) CV curves at 2 mV s^{-1} (**b**) CV curves of the RP$_{10}$G$_{90}$ fiber at different scan rates. (**c**) Dependence of the mass-specific capacitance on the scan rate. (**d**) EIS of all the fibers. (**e**) GCD curves of the RP$_{10}$G$_{90}$ fiber at different current densities. (**f**) Dependence of the mass- and volume-specific capacitance of the RP$_{10}$G$_{90}$ fiber on the current density.

Therefore, the RP$_{10}$G$_{90}$ fiber with the most appropriate amount of PVA demonstrates the best electrochemical performance.

The RP$_{10}$G$_{90}$ fiber exhibits a highest specific capacitance of 171 and 139 F g^{-1} at 2 and 5 mV s^{-1}, respectively. These values are significantly higher than that of a CNT-coated carbon fiber (~11 F g^{-1} at 2 mV s^{-1} in 1 M H$_2$SO$_4$) and a twist-spun CNT fiber (14.7 F g^{-1}, 5 mV s^{-1}, 0.5 M H$_2$SO$_4$) [53,54]. Further GCD tests (Fig. 7e) show that a specific capacitance as high as 216 F g^{-1} (241 F cm^{-3}) is achieved at a current density of 0.2 A g^{-1} (0.223 A cm^{-3}, 0.0852 mA cm^{-2}). This value is comparable with that of a CNT/RGO@CMC (carboxymethyl cellulose) coaxial hybrid fiber (239 F cm^{-3} at 0.1 mA cm^{-2}, 1 M H$_2$SO$_4$) and an electrolyte-mediated compact RGO film (255.5 F cm^{-3} at 0.1 A g^{-1}, 1 M H$_2$SO$_4$) [55,32]. It is worth noting that the cost of PVA is much lower than CNT and the spinning method is more convenience than coaxial spinning. When the current density increased to 2.0 A g^{-1} (2.23 A cm^{-3}), the specific capacitance reaches 105 F g^{-1} (117 F cm^{-3}), corresponding to a capacitance retention rate of 49%. This decrease is understandable, considering the moderate conductivity of the fiber and that no current collector was used for this long electrode (effective length = 1.5 cm).
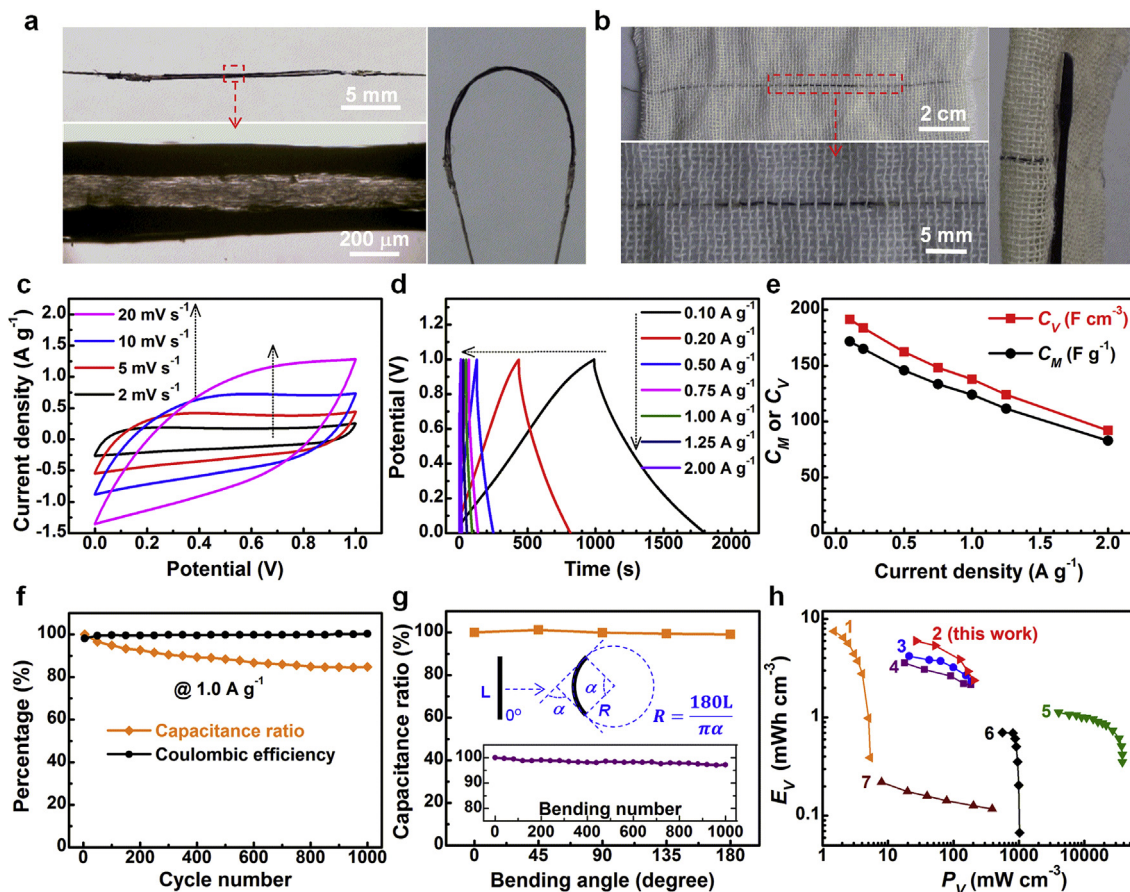
3.4. Performance of the PVA/RGO yarn supercapacitor

A flexible solid-state yarn supercapacitor was assembled from two bundles of RP$_{10}$G$_{90}$ fiber onto the substrate of a PET yarn in order to facilitate the weaving process and the electrical tests. As shown in Fig. 8a, the fibers in a single electrode bind together and attach well onto the PET yarn with the help of the PVA/H$_2$SO$_4$/H$_2$O gel electrolyte. This yarn supercapacitor shows excellent flexibility, and is robust enough to be woven into a textile (Fig. 8b). The CV curves (Fig. 8c) of this device are quasi-rectangular at low scan rates (≤10 mV s^{-1}), and the GCD curves (Fig. 8d) are near triangular with low potential drop at low current densities, indicating good charge propagation across the fibers. Based on the calculations from GCD curves, this yarn electrode exhibits a specific capacitance of 172 F g^{-1} (191 F cm^{-3}) and 165 F g^{-1} (184 F cm^{-3}) at the current

density of 0.1 A g^{-1} (0.112 A cm^{-3}, 0.043 mA cm^{-2}) and 0.2 A g^{-1} (0.223 A cm^{-3}, 0.0852 mA cm^{-2}) respectively. The coulombic efficiency (CE) is 82.5%, 87.0% and 97.9% at 0.1, 0.2 and 1.0 A/g, respectively. The low CE at low current density is possibly due to the partial electrolysis of water at high potential region and the irreversible oxidation of some functional groups on RGO sheets during charging. These capacitance values are significantly higher than that of a LC-spun RGO fiber (3.77 F cm^{-3} at 0.1 mA cm^{-2}) [13], a RGO core-sheath fiber (~38 F g^{-1} at 0.2 A g^{-1}) [12], and a RGO@CMC fiber (114 F cm^{-3} at 0.1 mA cm^{-2}) [32]. This yarn electrode is even superior to most graphene-based hybrid fiber electrodes such as a polyaniline deposited RGO fiber (76.1 F cm^{-3} at 0.1 mA cm^{-2}) [13], a MoS$_2$/RGO fiber (~120 F cm^{-3} at 0.1 A cm^{-3}) [31], a MnO$_2$ deposited RGO fiber (169 F cm^{-3} at 0.1 mA cm^{-2}) [33], and a CNT/RGO@CMC fiber (158 F cm^{-3} at 0.1 mA cm^{-2}) [32]. It is worth noting that the mechanical strength and the elongation at break of our RP$_{10}$G$_{90}$ fiber (186 MPa, 8.6%) are both higher than the above mentioned RGO core-sheath fiber (~156 MPa, ~2.1%), the RGO@CMC fiber (73 MPa, ~8%), the MnO$_2$ deposited RGO fiber (~125 MPa, ~4.2%), the CNT/RGO@CMC fiber (≤116 MPa), and the SWCNT/RGO fiber (≤165 MPa, <4%) [15], indicating much superior toughness for wearable applications.

When the current density is increased, the specific capacitance decreases to 124 F g^{-1} (138 F cm^{-3}) at 1.0 A g^{-1} and 82.7 F g^{-1} (92 F cm^{-3}) at 2.0 A g^{-1}, indicating a moderate capacitance retention rate of 72% and 48% respectively. This agrees well with that the CV curves turn into shuttle shapes at high scan rates (≥20 mV s^{-1}), which implies decreased capacitances during fast charge-discharge process. The reason might be due to the low conductivity and the dense structure of the RP$_{10}$G$_{90}$ fiber, limiting the electron transport and ion diffusion under high rate condition. The rate performance could possibly be improved by plying with a metal wire as the current collector in the future. The cycling stability was evaluated by cyclic GCD tests at 1.0 A g^{-1}. The coulombic efficiency increases from 98.1% to 100.2% after 1000 cycles, when the capacitance retention rate is 85% (Fig. 8f). The capacitance loss is also reported for other RGO fibers, CNT/RGO fibers and RGO films [20,52,58,59],

Fig. 8. Electrochemical performance of a yarn supercapacitor assembled from the RP$_{10}$G$_{90}$ fibers. (**a**) Photo of the device at straight and bending state. The enlarged part is an OM image of the device illustrating two bundle of hybrid fibers attached to a PET yarn. (**b**) Photo of the device weaved into a textile at relaxed and folded state. (**c**) CV curves at different scan rates. (**d**) GCD curves at different current densities. (**e**) Dependence of the volume- and mass-specific capacitance on the current densities. (**f**) Change of the capacitance ratio and coulombic efficiency during the GCD cycling at 1.0 A g^{-1}. (**g**) Capacitance change at different bending angles. The inset plot shows the capacitance stability during the cyclic bending between 0° to 180°. (**h**) Comparison of the volumetric energy and power densities of the device(2) with other wire-shaped supercapacitors based on the MoS$_2$/RGO fibers(3) [31], the CNT/RGO@CMC fibers(4) [32], the PEDOT/CNT fibers plied with Pt wires(5) [18], the MnO$_2$/carbon fibers (7) [7], as well as a commercial Li-film battery(1) [56] and a 2.75 V/44 mF active carbon supercapacitor(6) [57].

and may be ascribed to the gradual degradation of redox groups [52]. The flexibility of the yarn supercapacitor was investigated by measuring the capacitance stability under different bending angle (Fig. 8g). The result shows that 99% capacitance is remained when it is bent at 180°. And a 97% retention rate is observed after cyclic bending between 0° and 180° for 1000 times. This excellent flexibility and bending stability arise from the high toughness and strength of the RP$_{10}$G$_{90}$ fiber, and would be qualified for practical wearable applications.

The energy density and power density are two important parameters for supercapacitors, and their relationship can be featured in a Ragone plot [60]. Fig. 8h compares the Ragone plots of our yarn supercapacitor with other fiber supercapacitors and some commercial devices. The RP$_{10}$G$_{90}$ yarn supercapacitor possesses an energy density as high as 5.97 mW h cm^{-3} (5.32 mW h g^{-1}) at the power density of 26.9 mW cm^{-3}(23.9 mW g^{-1}). This value is superior to that of a MnO$_2$-deposited carbon fiber supercapacitor (0.22 mW h cm^{-3} at ~8 mW cm^{-3}) [7], a CNT/RGO fiber supercapacitor (3.4 mW h cm^{-3} at ~20 mW cm^{-3}) [58], a CNT/RGO@CMC fiber supercapacitor (3.5 mW h cm^{-3} at ~18 mW cm^{-3}) [32], and a MoS$_2$/RGO fiber supercapacitor (~4.2 mW h cm^{-3} at ~21 mW cm^{-3}) [31]. It is even comparable to that of a wire-shaped supercapacitor based on a hierarchical MnO$_2$/RGO hybrid fiber with 40 wt% MnO$_2$ nanowires (5.8 mW h cm^{-3} at ~23 mW cm^{-3}) [61]. Compared with

a Li-thin film battery, this yarn supercapacitor exhibits significantly higher power densities while holds comparable energy densities. Besides, these energy densities are ~7 times and ~3 times higher than those of a 2.75 V/44 mF active carbon supercapacitor and an ultrafast PEDOT/CNT fiber/Pt wire supercapacitor (1.4 mW h cm^{-3}, ~4000 mW cm^{-3}), respectively. Considering the power densities are inferior to the active carbon supercapacitor, future work will be focused on improving the rate performance.

4. Conclusion

In summary, continuous PVA/RGO hybrid fibers were successfully prepared by wet spinning of homogenous non-liquid-crystalline PVA/GO dispersion followed by chemical reduction. The hybrid fibers exhibit unique surface with plenty of nano wrinkles and different shaped cross-section with loosely stacked RGO sheets. Compared with the neat RGO fiber, their mechanical strength and toughness are significantly enhanced due to the gap-filling effect of PVA molecules as well as the strong interface interaction between PVA molecules and RGO sheets. The hydrophilicity is steadily increased with the increasing amount of hydrophilic PVA. Though less conductive than the neat RGO fiber, these hybrid fibers show enormous improvement in the electrochemical performance due to their unique surface morphology,

inner structure and enhanced hydrophilicity. The hybrid fiber prepared at a PVA/GO weight ratio of 10/90 performs best in 1 M H_2SO_4 and exhibits a specific capacitance of 241 F cm^{-3} at a current density of 0.223 A cm^{-3}, outperforming most graphene-based hybrid fibers. Moreover, its mechanical strength and toughness are simultaneously much higher than these hybrid fibers. A solid-state yarn supercapacitor assembled from the hybrid fibers demonstrates a device energy of 5.97 mW h cm^{-3}, together with excellent flexibility and bending-stability. This flexible device is also robust enough to be woven into a textile and hence has great potential as wearable power source for smart textiles.

Acknowledgements

References

[1] S. Park, S. Jayaraman, MRS Bull. 28 (2003) 585–591.
[2] D. Curone, E.L. Secco, A. Tognetti, G. Loriga, G. Dudnik, M. Risatti, R. Whyte, A. Bonfiglio, G. Magenes, IEEE Trans. Inf. Technol. Biomed. 14 (2010) 694–701.
[3] J. Rantanen, J. Impiö, T. Karinsalo, M. Malmivaara, A. Reho, M. Tasanen, J. Vanhala, Pers. Ubiquit. Comput. 6 (2002) 3–16.
[4] G.G. Wallace, T.E. Campbell, P.C. Innis, Fiber. Polym. 8 (2007) 135–142.
[5] A.B. Dalton, S. Collins, E. Muñoz, J.M. Razal, V.H. Ebron, J.P. Ferraris, J.N. Coleman, B.G. Kim, R.H. Baughman, Nature 423 (2003) 703.
[6] L. Yuan, X. Lu, X. Xiao, T. Zhai, J. Dai, F. Zhang, B. Hu, X. Wang, L. Gong, J. Chen, C. Hu, Y. Tong, J. Zhou, Z.L. Wang, ACS Nano 6 (2012) 656–661.
[7] X. Xiao, T. Li, P. Yang, Y. Gao, H. Jin, W. Ni, W. Zhan, X. Zhang, Y. Cao, J. Zhong, L. Gong, W. Yen, W. Mai, J. Chen, K. Huo, Y. Chueh, Z.L. Wang, J. Zhou, ACS Nano 6 (2012) 9200–9206.
[8] K. Jost, D. Stenger, C.R. Perez, J.K. McDonough, K. Lian, Y. Gogotsi, G. Dion, Energy Environ. Sci. 6 (2013) 2698–2705.
[9] K. Wang, Q. Meng, Y. Zhang, Z. Wei, M. Miao, Adv. Mater. 25 (2013) 1494–1498.
[10] J. Ren, L. Li, C. Chen, X. Chen, Z. Cai, L. Qiu, Y. Wang, X. Zhu, H. Peng, Adv. Mater. 25 (2013) 1155–1159.
[11] S.H. Aboutalebi, R. Jalili, D. Esrafilzadeh, M. Salari, Z. Gholamvand, S.A. Yamini, K. Konstantinov, R.L. Shepherd, J. Chen, S.E. Moulton, P.C. Innis, A.I. Minett, J.M. Razal, G.G. Wallace, ACS Nano 8 (2014) 2456–2466.
[12] Y.N. Meng, Y. Zhao, C.G. Hu, H.H. Cheng, Y. Hu, Z.P. Zhang, G.Q. Shi, L.T. Qu, Adv. Mater. 25 (2013) 2326–2331.
[13] T.Q. Huang, B.N. Zheng, L. Kou, K. Gopalsamy, Z. Xu, C. Gao, Y.N. Meng, Z.X. Wei, RSC Adv. 3 (2013) 23957–23962.
[14] X. Li, T. Zhao, K. Wang, Y. Yang, J. Wei, F. Kang, D. Wu, H. Zhu, Langmuir 27 (2011) 12164–12171.
[15] D.S. Yu, K. Goh, H. Wang, L. Wei, W.C. Jiang, Q. Zhang, L.M. Dai, Y. Chen, Nat. Nanotechnol. 9 (2014) 555–562.
[16] Y. Hu, H. Cheng, F. Zhao, N. Chen, L. Jiang, Z. Feng, L. Qu, Nanoscale 6 (2014) 6448–6451.
[17] Y. Chang, G. Han, D. Fu, F. Liu, M. Li, Y. Li, J. Power Sources 252 (2014) 113–121.
[18] J.A. Lee, M.K. Shin, S.H. Kim, H.U. Cho, G.M. Spinks, G.G. Wallace, M.D. Lima, X. Lepro, M.E. Kozlov, R.H. Baughman, S.J. Kim, Nat. Commun. 4 (2013) 1970.
[19] Z. Xu, C. Gao, Nat. Commun. 2 (2011) 571.
[20] S. Chen, W. Ma, Y. Cheng, Z. Weng, B. Sun, L. Wang, W. Chen, F. Li, M. Zhu,

[21] H. Cheng, Nano Energy 15 (2015) 642–653.
[21] Y. Zhao, C. Jiang, C. Hu, Z. Dong, J. Xue, Y. Meng, N. Zheng, P. Chen, L. Qu, ACS Nano 7 (2013) 2406–2412.
[22] Y. Zhu, S. Murali, M.D. Stoller, K.J. Ganesh, W. Cai, P.J. Ferreira, A. Pirkle, R.M. Wallace, K.A. Cychosz, M. Thommes, D. Su, E.A. Stach, R.S. Ruoff, Science 332 (2011) 1537–1541.
[23] Z. Lei, N. Christov, X.S. Zhao, Energy Environ. Sci. 4 (2011) 1866–1873.
[24] G.P. Hao, A.H. Lu, W. Dong, Z.Y. Jin, X.Q. Zhang, J.T. Zhang, W.C. Li, Adv. Energy Mater. 3 (2013) 1421–1427.
[25] H.J. Fei, C.Y. Yang, H. Bao, G.C. Wang, J. Power Sources 266 (2014) 488–495.
[26] X.W. Yang, J.W. Zhu, L. Qiu, D. Li, Adv. Mater. 23 (2011) 2833–2838.
[27] Y. Chen, X. Zhang, D. Zhang, P. Yu, Y. Ma, Carbon 49 (2011) 573–580.
[28] C.T. Hsieh, S.M. Hsu, J.Y. Lin, Jpn. J. Appl. Phys. 51 (2012) 01AH06.
[29] Y. Yu, Y. Sun, C. Cao, S. Yang, H. Liu, P. Li, P. Huang, W. Song, J. Mater, Chem. A 2 (2014) 7706–7710.
[30] Q. Chen, Y. Meng, C. Hu, Y. Zhao, H. Shao, N. Chen, L. Qu, J. Power Sources 247 (2014) 32–39.
[31] G.Z. Sun, J.Q. Liu, X. Zhang, X.W. Wang, H. Li, Y. Yu, W. Huang, H. Zhang, P. Chen, Angew. Chem. Int. Ed. 53 (2014) 12576–12580.
[32] L. Kou, T.Q. Huang, B.N. Zheng, Y. Han, X.L. Zhao, K. Gopalsamy, H.Y. Sun, C. Gao, Nat. Commun. 5 (2014) 3754.
[33] B.N. Zheng, T.Q. Huang, L. Kou, X.L. Zhao, K. Gopalsamy, C. Gao, J. Mater, Chem. A 2 (2014) 9736–9743.
[34] S. Zhang, L. Zhu, C. Wong, S. Kumar, Macromol. Rapid Comm. 30 (2009) 1936–1939.
[35] S. Zhang, W. Lin, C. Wong, D.G. Bucknall, S. Kumar, ACS Appl. Mater. Inter 2 (2010) 1642–1647.
[36] P. Miaudet, S. Badaire, M. Maugey, A. Derre, V. Pichot, P. Launois, P. Poulin, C. Zakri, Nano Lett. 5 (2005) 2212–2215.
[37] K. Liu, Y. Sun, X. Lin, R. Zhou, J. Wang, S. Fan, K. Jiang, ACS Nano 4 (2010) 5827–5834.
[38] L. Kou, C. Gao, Nanoscale 5 (2013) 4370–4378.
[39] W.S. Hummers Jr., R.E. Offeman, J. Am. Chem. Soc. 80 (1958) 1339.
[40] S. Pei, J. Zhao, J. Du, W. Ren, H.M. Cheng, Carbon 48 (2010) 4466–4474.
[41] S.H. Aboutalebi, M.M. Gudarzi, Q.B. Zheng, J.K. Kim, Adv. Funct. Mater. 21 (2011) 2978–2988.
[42] Z. Xu, C. Gao, ACS Nano 5 (2011) 2908–2915.
[43] R. Jalili, S.H. Aboutalebi, D. Esrafilzadeh, R.L. Shepherd, J. Chen, S. Aminorroaya-Yamini, K. Konstantinov, A.I. Minett, J.M. Razal, G.G. Wallace, Adv. Funct. Mater. 23 (2013) 5345–5354.
[44] H. Bai, C. Li, X. Wang, G. Shi, Chem. Commun. 46 (2010) 2376–2378.
[45] J.J. Liang, Y. Huang, L. Zhang, Y. Wang, Y.F. Ma, T.Y. Guo, Y.S. Chen, Adv. Funct. Mater. 19 (2009) 2297–2302.
[46] X. Zhao, Q. Zhang, D. Chen, P. Lu, Macromolecules 43 (2010) 2357–2363.
[47] L.W. Wang, R.J. Liao, Z.H. Tang, Y.D. Lei, B.C. Guo, J. Phys. D. Appl. Phys. 44 (2011), 44530244.
[48] T. Zhou, F. Chen, C. Tang, H. Bai, Q. Zhang, H. Deng, Q. Fu, Compos. Sci. Technol. 71 (2011) 1266–1270.
[49] A. Lewandowski, M. Galinski, Pol. J. Chem. 75 (2001) 1913–1920.
[50] C. Meng, C. Liu, L. Chen, C. Hu, S. Fan, Nano Lett. 10 (2010) 4025–4031.
[51] A. Khosrozadeh, M. Xing, Q. Wang, Appl. Energy 153 (2015) 87–93.
[52] Y.J. Oh, J.J. Yoo, Y.I. Kim, J.K. Yoon, H.N. Yoon, J.H. Kim, S.B. Park, Electrochim. Acta 116 (2014) 118–128.
[53] T.L. Viet, H. Kim, A. Ghosh, J. Kim, J. Chang, A.V. Quoc, T.P. Duy, J. Lee, S. Kim, Y.H. Lee, ACS Nano 7 (2013) 5940–5947.
[54] X. Lepro, R. Ovalle-Robles, M.D. Lima, A.L. Elias, M. Terrones, R.H. Baughman, Adv. Funct. Mater. 22 (2012) 1069–1075.
[55] X.W. Yang, C. Cheng, Y.F. Wang, L. Qiu, D. Li, Science 341 (2013) 534–537.
[56] D. Pech, M. Brunet, H. Durou, P.H. Huang, V. Mochalin, Y. Gogotsi, P.L. Taberna, P. Simon, Nat. Nanotechnol. 5 (2010) 651–654.
[57] M.F. El-Kady, V. Strong, S. Dubin, R.B. Kaner, Science 335 (2012) 1326–1330.
[58] Y. Ma, P. Li, J.W. Sedloff, X. Zhang, H. Zhang, J. Liu, ACS Nano 9 (2015) 1352–1359.
[59] R. Ramachandran, M. Saranya, V. Velmurugan, B.P.C. Raghupathy, S.K. Jeong, A.N. Grace, Appl. Energy 153 (2015) 22–31.
[60] T. Christen, M.W. Carlen, J. Power Sources 91 (2000) 210–216.
[61] W. Ma, S. Chen, S. Yang, W. Chen, Y. Cheng, Y. Guo, S. Peng, S. Ramakrishna, M. Zhu, J. Power Sources 306 (2016) 481–488.